Assessing depth sensitivity in laser interferometry speckle visibility spectroscopy (iSVS) through source-to-detector distance variation and cerebral blood flow monitoring in humans and rabbits

SIMON MAHLER,[1,*] **YU XI HUANG,**[1] **MINGSHU LIANG,**[1] **ALAN AVALOS,**[2] **JULIAN M. TYSZKA,**[3] **JEROME MERTZ,**[4,5] **AND CHANGHUEI YANG**[1]

[1]*Department of Electrical Engineering, California Institute of Technology, Pasadena, California 91125, USA*
[2]*Office of Laboratory Animal Resources (OLAR), California Institute of Technology, Pasadena, California 91125, USA*
[3]*Division of Humanities and Social Sciences, California Institute of Technology, Pasadena, California 91125, USA*
[4]*Department of Biomedical Engineering, Boston University, Boston, Massachusetts 02215, USA*
[5]*Neurophotonics Center, Boston University, Boston, Massachusetts 02215, USA*
[*]*sim.mahler@gmail.com*

Abstract: Recently, speckle visibility spectroscopy (SVS) was non-invasively applied on the head to monitor cerebral blood flow. The technique, using a multi-pixel detecting device (e.g., camera), allows the detection of a larger number of speckles, increasing the proportion of light that is detected. Due to this increase, it is possible to collect light that has propagated deeper through the brain. As a direct consequence, cerebral blood flow can be monitored. However, isolating the cerebral blood flow from the other layers, such as the scalp or skull components, remains challenging. In this paper, we report our investigations on the depth-sensitivity of laser interferometry speckle visibility spectroscopy (iSVS). Specifically, we varied the depth of penetration of the laser light into the head by tuning the source-to-detector distance, and identified the transition point at which cerebral blood flow in humans and rabbits starts to be detected.

1. Introduction

Measuring blood flow on the head is an indirect way to access or quantify brain activity. For example, it is useful for diagnosing traumatic brain injuries by looking at the changes of blood flow [1–3]. However, measuring the cerebral blood flow (CBF) remains challenging. The principal difficulty lies in the ability to reach and collect signal from the brain noninvasively, where the collected signal from the brain layer must be separated from the signal of other layers, such as the scalp and skull. Many input sources and approaches have been tested for this purpose, including Magnetic Resonance Imaging (MRI) [3–7], electrophysiology [7], ultrasound [8–10], spectroscopy [11–19], or laser speckle [20–26]. The challenge in developing such a device is that the proportion of light detected is limited by the low number of collected signal interacting with the brain, especially for biomedical applications where the exposure and emission levels are restricted for the safety of the subjects [27].

Diffusing wave spectroscopy, utilizing light transmitted through a scattering medium to extract the dynamics, has recently drawn attention for monitoring CBF [28–35]. It has the advantage that many photons interacting with the brain can be collected. In addition, laser-based devices

can be designed in a low-cost, and compact manner. To measure CBF, laser light is directed into the head using a laser source, and the emerging light is collected by a detector positioned at a source-to-detector (S-D) separation distance from the injection spot. The movements of blood cells within the travelling light's path will scatter and change the effective optical path lengths, resulting in a fluctuating laser speckle field. There exist two types of sampling techniques to infer the blood flow: temporal and spatial.

The temporal sampling technique, called diffuse correlation spectroscopy [13–19], is based on the use of the temporal ensemble of the speckle field and diffusing wave spectroscopy. The temporal sampling method uses a detecting device working at a high frame rate (typically above 100 kHz) on a single (or on a small group of) speckle, such that the inverse of the frame rate is shorter than the decorrelation time of the speckle field. In this configuration, the decorrelation time of the recorded signal can be calculated and related to the blood flow level.

The spatial sampling technique is based on the use of spatial ensemble of the speckle field, usually referred as speckle visibility spectroscopy (SVS) [20,28,29], or multi-speckle diffuse wave spectroscopy [30–33] or laser speckle contrast optical spectroscopy [21–26,34]. Here, instead of a high frame rate detecting device, a camera with many pixels is used to collect more photons within the same frame. The camera is typically working at an exposure time longer than the decorrelation time of the speckle field. This results in multiple different speckle patterns summing up onto a single camera frame. As the speckle field fluctuates, the speckle pattern recorded by the camera is smeared and washed out within the exposure time [28,29]. The smearing or washing out is due to the dynamics of the blood cells, thus the decorrelation time can be calculated from the degree of blurring of the captured frame, typically by calculating the speckle contrast. There is a slightly different and more advanced form of SVS, called interferometric SVS (iSVS) [29,35], where a reference light field is introduced to enable interferometric detection of the weak diffused light [29,35–38].

iSVS was recently applied on the head to monitor blood flow, allowing the detection of a larger number of speckles, increasing the proportion of detected light. Due to this increase, it is possible to collect light that has propagated deeper through the brain. As a direct consequence, CBF can be monitored in iSVS [29]. However, effectively isolating the CBF from the other layers, such as the scalp or skull components, remains challenging. The depth to which the photons travelled in the head is intrinsically related to the S-D separation distance [39–43]. The chief advantage of using a source-to-detector scheme is that the depth of penetration of the laser light into the sample can be tuned by varying the source-to-detector distance.

Recently, functional interferometric diffusing wave spectroscopy (iDWS) was employed to assess and monitor brain signals in humans, driven either by neural activity or cerebrovascular reactivity [32]. Brain-to-scalp sensitivity was shown to follow a double-layer decay model as the pulsatile blood flow index changed with varying S-D distances from 1 to 4 cm [32].

In this paper, we report our investigations on the depth-sensitivity of laser interferometry speckle visibility spectroscopy (iSVS). Building upon insights from previous iDWS [31,32] and NIRS [39–43] simulations and experiments, we conducted an experimental investigation into the depth sensitivity of iSVS, employing the spatial ensemble of the speckle field. The primary objective was to identify the specific transition point at which cerebral blood flow becomes detectable both in humans and rabbits. Specifically, we varied the depth of penetration of the laser light into the head by tuning the source-to-detector distance and identified the transition point at which CBF in humans and rabbits start to be detected. Our skin-to-brain depth results from iSVS agree with the MRI and X-rays scans, both for humans and rabbits.

2. Experimental arrangement

The experimental arrangement for laser interferometry speckle visibility spectroscopy (iSVS) is shown in Fig. 1 [29,35]. It is based on an off-axis Mach-Zehnder interferometer. For this

study, we used a single-mode, single-frequency continuous wave 785 nm laser source [Thorlabs FPV785S & CLD1015]. This laser source has a long (>5 m) coherence length, useful for interferometry, is thermally stabilized and can deliver up to 50 mW, useful for laser speckle imaging. The arrangement in Fig. 1(a) is set as follow: the input laser beam is divided by a 10:90 (Reflectivity:Transmission) beam splitter [Thorlabs BS044] into two light beams: one light beam for illuminating the sample (sample arm) and one light beam for interfering with the sample laser light beam (reference arm).
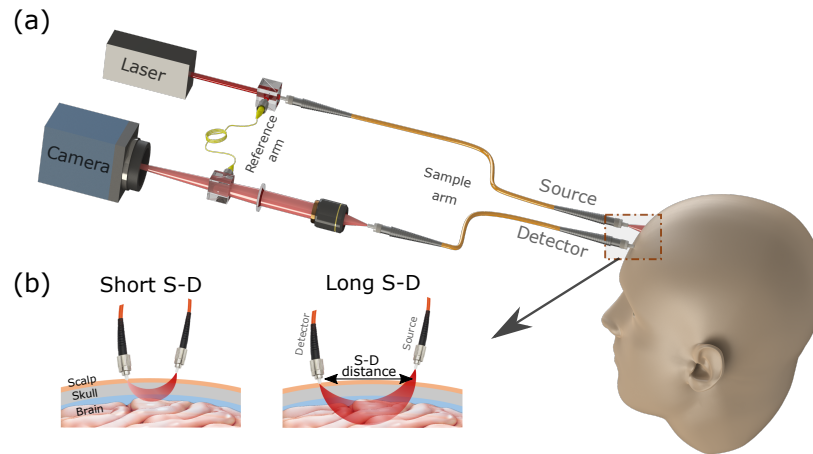

Fig. 1. (a) Experimental arrangement of laser interferometry Speckle Visibility Spectroscopy (iSVS). In this case, the subject is a human. (b) Example of iSVS depth sensitivity by varying the Source-to-Detector (S-D) distance. As evident, the depth of penetration increases with the S-D distance [39–43].

In the reference arm, the laser light is coupled into a single mode fiber [Thorlabs SM800-5.6-125]. The use of a single mode fiber allows us to generate a circular Gaussian-beam at the output. It also allows us to match the pathlength of the reference arm with the pathlength of the sample arm by choosing the appropriate fiber length. The other end of the single mode fiber illuminates a second 10:90 (R:T) beam splitter [Thorlabs BS044] and the reference laser light is directed onto a scientific CMOS camera [Excelitas pco.edge 5.5] with a pixel size of 6.5×6.5 μm.

In the sample arm, the laser light is coupled into a 600 μm core diameter multimode fiber [Thorlabs FT600UMT]. The other end of the multimode fiber is set a few millimeters away from the sample (e.g. human or rabbit head), such that the laser light intensity level of the area of illumination is well within the American National Standards Institute (ANSI) laser safety standards of 2.96 mw/mm^2 for maximum permissible exposure for skin exposure to a laser beam at 785 nm [27].

At a separation distance S-D from the illumination fiber, a multimode fiber with a 600 μm core diameter [Thorlabs FT600UMT] collects the laser light that propagated inside the head of the subject, see Fig. 1(b). By tuning the S-D distance, one can tune the depth of penetration into the head of the subject, see Fig. 1(b) [41–43]. The collected laser light is imaged onto the camera.

To optimize the interferometric measurement, neutral density (ND) filters [Thorlabs NEXXA-B] and shutters [Picard Industries USB Optical Shutter] can be used to reduce or to block the laser light intensity in the sample or in the reference arm. The optical fibers were taped onto the optical table and securely fastened to prevent any slight movements that could potentially introduce speckle artifacts. At the second beam splitter, the reference and sample arm laser light beams interfere and form an interference pattern recorded by the camera with a speckle to pixel size of about 2×2 pixels.

The camera in Fig. 1(a) was recording at a rate of 50-100 frames per second and with an exposure time T of either 0.5 ms (Figs. 2, 3 and 4(a)) or 1 ms (Fig. 4(b)). The recorded images by the camera are processed digitally, as shown in Fig. 2. For a more accurate measurement, the recorded images (Fig. 2(a)) are calibrated by subtracting them with a reference arm only laser light image (Fig. 2(b)). To get the reference arm laser light, the sampling laser light beam was blocked (at $t = 0$) and the reference arm laser light was measured from an average over 50 images to reduce shot noise and camera noise effect.
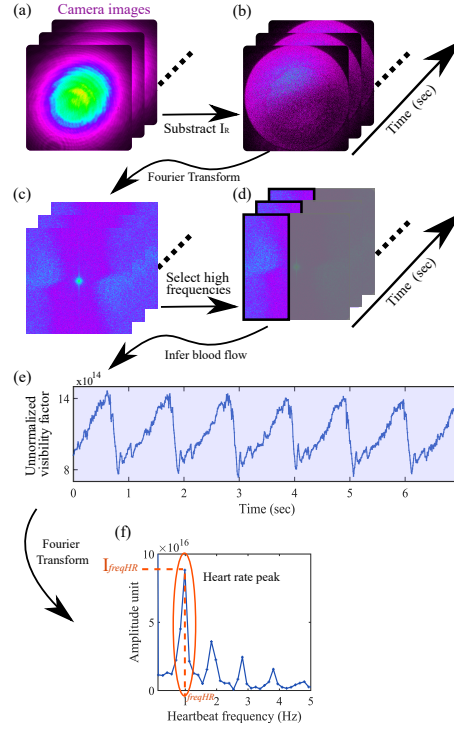

Fig. 2. Interferometric speckle visibility spectroscopy (iSVS) processing pipeline. (a) A series of interference pattern images are recorded by the camera in Fig. 1. (b) The camera images are calibrated by subtracting the reference intensity. (c) Fourier transform of the calibrated images in (b). (d) The high-frequency interference lobe, which carries blood flow signal information, is selected. (e) The temporal dynamics of the blood flow is inferred by integrating the high-frequency lobe in (d). (f) By Fourier transforming the blood flow dynamics in (e), the heart rate Fourier peak can be identified. The frequency *freqHR* corresponds to the heart rate (in Hertz) and the amplitude I_{freqHR} indicates the reconstruction quality of the blood flow signal in (e).

The instantaneous intensity at the camera at pixel j can be expressed as [29,35,44]:

$$I_j(t) = I_{Sj}(t) + I_{Rj} + 2\sqrt{I_{Sj}(t)I_{Rj}} \cos(\phi_{Rj} - \phi_{Sj}(t))exp\left[-\left(\frac{\Delta L}{l_c}\right)^2\right] + n_j(t), \qquad (1)$$

where in Eq. (1), $I_{Sj}(t)$ *is* the sample arm intensity ($\phi_{Sj}(t)$ the phase) at pixel j, I_{Rj} the reference arm intensity (ϕ_{Rj} the reference phase containing off-axis adjustments), the third term is the interference cross term, and $n_j(t)$ the noise term including shot noise, camera noise and laser noise, see Refs. [29,35]. The coherence length l_c of the incident laser beam and the path-length difference ΔL between the sample and reference arm of the interferometer were included in the

(a) SVS (Speckle Visibility Spectroscopy)
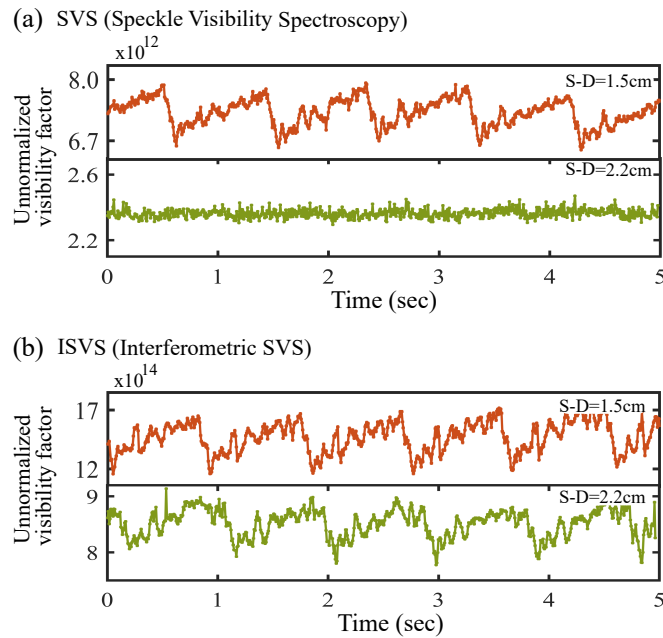

(b) ISVS (Interferometric SVS)

Fig. 3. Human blood flow measurement comparison between (a) SVS and (b) iSVS detection methods. As evident, iSVS typically produces blood flow with better reconstruction quality than SVS.
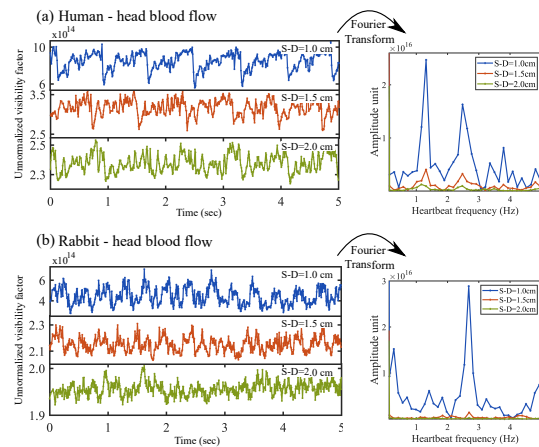

Fig. 4. Measured blood flow at different source-to-detector (S-D) distances on (a) human head, and (b) rabbit head. As evident, the quality of reconstruction of the blood flow dynamics decreases as the S-D distance increases, both for human and rabbit.

equation by using Eq. (6) of [45] and Eq. (4) of [46]. For the following, we assume $\Delta L << l_c$, such that $\exp\left[-\left(\frac{\Delta L}{l_c}\right)^2\right] \approx 1$.

By subtracting the reference, and assuming $I_{Rj} \gg I_{Sj}$, the signal recorded by the camera for a single frame is given by:

$$N_j = \frac{1}{T}\int_0^T \sqrt{I_{Sj}(t)I_{Rj}}\ exp(i\phi_j)dt, \tag{2}$$

with ϕ_j the phase difference between the reference laser beam and the sample laser beam light field [29].

The visibility factor F is defined as:

$$F = \frac{\langle|N_j|^2\rangle}{I_S I_R} = \frac{1}{T}\int_0^T 2\left(1 - \frac{t}{T}\right)g_1(t)dt, \tag{3}$$

with N_j the iSVS signal, $\langle\cdot\rangle$ the expected value, $I_S I_R$ the normalization factor composed of the averaged reference arm intensity I_R and the averaged sample arm intensity I_S, T is the exposure time of the camera, and g_1 is the field decorrelation function. See Sec. D in the Supplementary Note of [29] for full derivation.

The above derivation assumes well behaved camera and laser noises that can be characterized and corrected. In practical applications, achieving such ideal conditions may pose challenges. If we are interested in measuring the dynamical change in F as a way to gauge blood flow changes, we can compute an unnormalized visibility factor (relative measurement of $\langle|N_j|^2\rangle$ in Eq. (3)) by Fourier transforming each recorded image (Fig. 2(c)) and integrating the high-frequency interference lobe (Fig. 2(d)). By integrating the high-frequency interference lobe (third term of Eq. (1)), which carries the reference enhanced blood flow signal information, we can effectively filter out the spatial low-frequency noise.

The temporal dynamics of the blood flow was measured via the computation of an unnormalized visibility factor, Fig. 2(e). The time information was retrieved from the camera time stamps. As show in Fig. 2(e), blood flow can be monitored on the head. The heart rate of the subject can be calculated by Fourier transforming the blood flow signal, Fig. 2(f).

In Fig. 2(f), the Fourier amplitude peak centered around $freqHR = 1.0\,\text{Hz}$ corresponds to the heart rate amplitude peak of the subject. There are also Fourier peaks centered at 1.8 Hz and 2.8 Hz in Fig. 2(f), corresponding to the second and third sub-harmonics of the heart rate pulsations of the subject.

Note that it is also possible to use iSVS for monitoring relative changes in oxygenation levels. However, since iSVS only uses a single wavelength, absolute oxygenation is difficult to obtain. The intensity of the recorded images allows for the possibility of measuring relative fluctuations in oxygenation.

For this study, we recruited participants from the Caltech and Pasadena community, recruited among healthy adult human aged from 21 to 65 years. The human research protocol for this study received approval from the Caltech Institutional Review Board. For this study, three human subjects were recruited. The first two subjects were comfortable with shaving their heads. To accommodate the third subject, iSVS study was conducted on areas without hair, such as the forehead or frontotemporal area of the head. Two rabbits participated in the experiments and had their heads shaved.

To compare with the iSVS laser results, MRI scans of the head of the human subjects were done at the Caltech Brain Imaging Center and X-rays of the head of the rabbits were done at the Caltech Animal Facility Center.

Structural MRI data were acquired at the Caltech Brain Imaging Center using a 3 Tesla MRI scanner (Prisma Fit model manufactured by Siemens Medical Solutions, Malvern PA) with a 32-channel head receive array. T1-weighted images were acquired with the following parameters:

3D MEMP-RAGE sequence, TR 2550 ms, TE 1.6, 3.5, 5.3, 7.1 ms, TI 1150 ms, 0.9 mm isotropic voxels. T2-weighted images were acquired with the following parameters: 3D T2w SPACE sequence, TR 3200 ms, effective TE 564 ms, 0.9 mm isotropic voxels. Pial surface estimates and skin-to-brain depths were generated using Freesurfer 7.2.

The animal research protocol for the rabbits' study received approval by the Caltech Institutional Animal Care and Use Committee. The two rabbits were 4-month-old male New Zealand White rabbits. Throughout the experiments, the rabbits were kept under anesthesia with the help of a veterinary team to ensure their comfort and safety. Anesthesia induction was achieved using an injectable mixture of ketamine (35 mg/kg) and xylazine (5 mg/kg), administered in a single intramuscular injection in the epaxial muscles, and was maintained with 1.5% to 2% isoflurane gas anesthesia delivered by oxygen and administered via a nose cone. The use of the nose cone for anesthesia delivery may result in occasional short periods of awakening for the rabbit during the experiments.

To compare the human and rabbit results, we designed a phantom. Our phantom comprised of a liquid mixture in a plastic cup, placed on an orbital shaker rotating at a 60 rotations per minute speed, see Appendix A for more details. The source and detector fibers were mounted on a separate support above the cup, which was not moving, see sketch in Fig. 7(a). The iSVS system is measuring the difference of angular velocities along the horizontal line of the rotating liquid mixture, producing a liquid flow dynamic similar to the blood flow dynamic for humans, see Fig. 7(e). For the phantom experiments, one phantom was made of 3% fat-milk and another phantom was made with a mixture of 10% 3D printing resin and 90% water.

For this study, iSVS was preferred over SVS due to the better depth sensitivity, as shown in Fig. 3, but our findings and conclusions are also valid for SVS as long as the system can provide adequate proportion of detected light to resolve the cardiac pattern of the blood flow. To conduct the SVS measurement, the laser light intensity in the reference arm was blocked, allowing only the laser light emitted from the sample arm [35].

3. Results

The peaks observed in the visibility spectrum of Fig. 2(f) serve as reliable indicators of the quality of blood flow signal reconstruction. The frequency *freqHR*, as defined in Fig. 2(f), corresponds to the heart rate of the subject and its amplitude I_{freqHR} indicates the reconstruction accuracy of the blood flow signal. By examining the amplitude of the Fourier peak corresponding to the heart rate I_{freqHR} in the visibility spectrum, variations in reconstruction quality can be detected with greater precision than by observing intensity fluctuations in the reconstructed blood flow or by measuring the amount of light collected, $I_S(t)$. For example, Fig. 4 shows the CBF at three different S-D distances of 1.0 cm, 1.5 cm and 2.0 cm for human in Fig. 4(a) and for rabbit in Fig. 4(b). Note that the heart rate for a human at rest/sleep is typically in the range 0.7-1.5 Hz, while the rabbit heart rate at rest/sleep is typically in the range 2.3-3.5 Hz.

In Fig. 4, as the S-D distance increases, the accuracy of the reconstruction of the blood flow is diminished. For instance, in Fig. 4(a), at S-D = 1.0 cm, the heart rate pulse is easily identified on the left graph. However, at S-D = 2.0 cm, the heart rate pulse becomes less distinct. To quantify this difference in signal quality, we examine the visibility spectrum on the right graph, which is the Fourier transform of the measured blood flow. As the measured blood flow's signal quality diminishes, the amplitude of the heart rate pulse progressively reduces.

As evident in Fig. 4 right column, I_{freqHR} decreases as the S-D distance increases, while the heart rate frequency *freqHR* remains the same. This can be explained by the fact that when the S-D distance increases, the depth of penetration also increases, as shown in Fig. 1(b). As the depth of penetration increases, the laser light travelling distance increases, experiencing a larger scattering process, as shown in Fig. 1(b). Then, the number of photons collected back by the detector decreases, as well as the accuracy of the measurement and the reconstructed blood flow.

By increasing the S-D distance and measuring the quality of reconstruction of the blood flow, one should observe a double decay curve. This double decay curve arises due to the presence of various head components, namely the scalp + skull layer and the dura mater + brain layer. At short S-D distances, the decay curve corresponds to the absorption and scattering characteristics of the scalp + skull components. Subsequently, as the S-D distance extends further, a different decay curve emerges when the brain component is probed. This differentiation is attributed to the differing optical properties, i.e., absorption and scattering coefficients, between the dura mater + brain and scalp + skull components [32,35], leading to the observation of a double decay curve [39–43].

It is important to note that this phenomenon primarily impacts the quality of blood flow reconstruction I_{freqHR}, and not the frequency *freqHR* or the pulsation of the blood flow, as both the scalp + skull and dura mater + brain components of the head respond to the same cardiac pulse. Another potential reason for observing the double decay curve lies in the variation of capillary beds between the scalp + skull and dura mater + brain layers of the head.

By measuring the threshold point between the two decay slopes, one can infer the S-D distance at which the iSVS system starts measuring CBF. To verify our hypothesis, we performed experiments on human heads, rabbit heads and simplistic phantoms composed of a moving liquid, as shown in Fig. 5. Both humans and rabbits have a similar head structure that can be modelled as a two-layer phantom with a scalp + skull layer and a dura mater + brain layer. However, the human head is larger than the rabbit head. Thus, the depth of penetration needed to reach the dura mater + brain layer is longer with humans than for rabbits. Our phantom comprised of a liquid mixture in a plastic cup, placed on an orbital shaker rotating at a 60 rotations per minute speed, see Appendix A for more details.

The results are shown in Fig. 5 for (a) human head, (b) rabbit head and (c) liquid mixture phantom. For each subject, the S-D distance was varied in the range 0.5-3.2 cm with a 0.1 cm increment. At each S-D distance, the blood flow of the subject was measured for a period of eight seconds. Then, the amplitude I_{freqHR} and frequency *freqHR* were calculated. For each S-D distance, the results were averaged over five different realizations. The error-bars in Fig. 5 correspond to the standard-deviation of the results from the five different realizations. Approximately, each realization took about 20 sec to be recorded and saved. The recording time for a full scan (e.g., Fig. 5(a)) was about 30 min. During this time, the subject was laying down on a massage table and was asked to relax, meditate and to not move their head. For the rabbit experiments, the rabbit was put under anesthesia.

As shown in Fig. 5, left column, I_{freqHR} follows a double decay slope for both human and rabbit, while it follows a single decay slope for phantom. We define the slope of the first decay curve as a_1 and the slope of the second decay curve as a_2. As evident, both for human and rabbit, the first decay rate is higher than the second decay rate, $a_1 >> a_2$. This can be interpreted in two ways. One is that iSVS system experience more optical loss from the scalp + skull layer than with the dura mater + brain layer, as the S-D distance is increasing (less photons are captured). Another would be that the brain blood flow is higher, creating more fluctuations in the blood flow measurements, such that the decay of the amplitude of fluctuation slows down after reaching brain.

Contrasting these results, the phantom experiment (Fig. 5(c)), which involves diluted resin in water, shows a single decay corresponding to the presence of a single liquid layer. In this scenario, there are no complex tissue layers with varying optical properties, and thus, the decay of I_{freqHR} follows a single decay.

The corresponding heart rate frequencies *freqHR* are shown in the right column of Fig. 5. For human, the frequency fluctuates around 1.2 Hz all over the span of the scan (30 min period), corresponding to a normal heart rate for a resting/meditating human. For rabbit head, due to the anesthesia, the frequency is very stable over the 30 minutes scan, at around 2.7 Hz, except
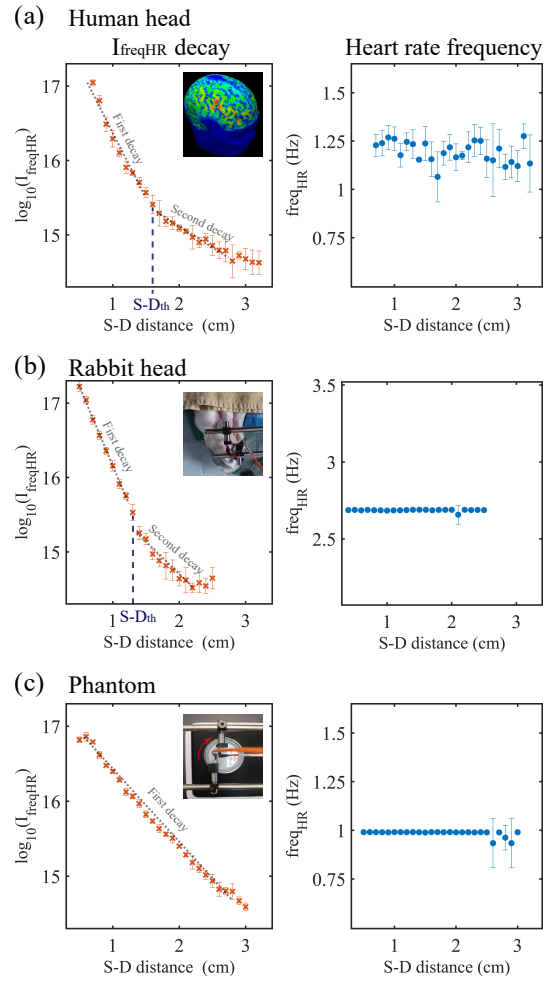
Fig. 5. Investigating the threshold Source-to-Detector (S-D) distance at which iSVS system starts to reach the brain component of the subject. (a) Human head, (b) rabbit head and (c) phantom. In (a) and (b), there is a double decay. The first decay, with slope rate a_1, corresponds to the scalp + skull layer and the second decay with a slope rate a_2 to the dura mater + brain layer. For the phantom (diluted resin in water) in (c), there is a single decay corresponding to the single liquid layer.

for a few datapoints when the rabbit temporarily awoke. Due to the limited time window from the anesthesia, the maximal S-D distance for the rabbit study that we were able to measure was 2.8 cm.

For the phantom, the frequency *freqHR* is 1 Hz for all S-D distances until 2.6 cm. For S-D distances above 2.6 cm, the measured flow suffers from noise to produce good reconstruction results. This indicates that the S-D distance of 2.6 cm for the phantom corresponds the maximal range of flow measurement for our 785 nm iSVS system. Similarly, we measured the maximal S-D distance at which blood flow can be reconstructed to be 2.8-3.0 cm for human studies and 2.5-2.8 cm for rabbit studies at 785 nm iSVS system. The difference between human and rabbit is because the rabbit head is smaller than human, so the brain layer is attained at a shorter S-D distance for rabbits.

These results support our hypothesis that by tuning the S-D distance across a scanning line, it is then possible to measure the source-to-detector threshold distance (S-D_{th}) at which brain signal can be detected. For example, in Fig. 5(a) S-D_{th} = 1.6 cm and in Fig. 5(b) S-D_{th} = 1.3 cm. The results in Figs. 4 and 5 were recorded from subject Human1 and Rabbit1.

Next, we repeated the experiments at N different locations on the head of different subjects Human1, Human2 and Human3 and subjects Rabbit1 and Rabbit2. The skin-to-brain depth varies from different regions of the human head, directly affecting the measured S-D_{th}. For those reasons, we measured the skin-to-brain depth (via MRI/X-rays scans) and S-D_{th} (via iSVS measurements) separately at N different regions of the head for each subject. The statistics were grouped for each subject and presented in Fig. 6(a) for the skin-to-brain depth, and in Fig. 6(b) for the S-D_{th}.

For example, N = 9 different measurements were done for Human1 and the results were grouped and presented by showing the mean, the maximum, the minimum, the quartile1 and the quartile3, Fig. 6. The grouping of the measurements gives an overall estimation of the skin-to-brain distance of each subject. Such overall estimation helps in comparing the skin-to-brain distances measured from MRI scans for humans (or X-rays scan for rabbits) with the measured S-D_{th}. The MRI scans of the head of the human subjects were done at the Caltech Brain Imaging Center and the X-rays of the head of the rabbits were done at the Caltech Animal Facility Center. The results are presented in Fig. 6.

Figure 6(a) shows the averaged skin-to-brain depth *z* of each subject, measured from the MRI and X-rays scans. Figure 6(b) shows the measured threshold S-D_{th} distance from the iSVS blood flow measurements (as in Fig. 5). As shown, the skin-to-brain depths estimated from the MRI and X-rays scans agree with the iSVS S-D_{th} distances, where the S-D_{th} distances for humans are larger than for rabbits. In addition, the MRI results show that the skin-to-brain depth of Human3 is slightly larger than Human1 and Human2, Fig. 6(a), which was also observed in Fig. 6(b).
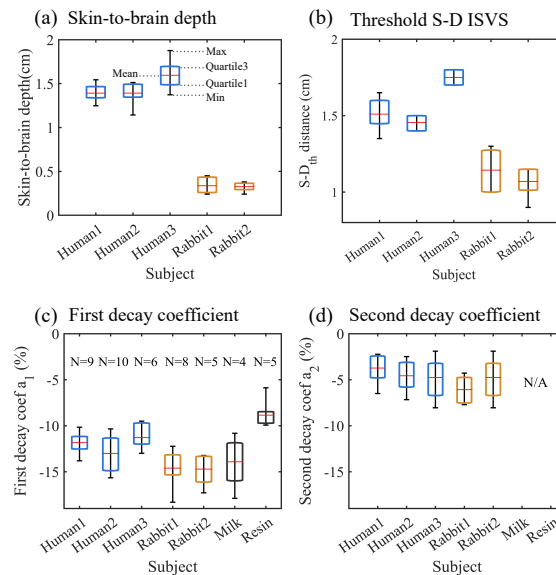

Fig. 6. (a) and (b) Estimating the threshold S-D distance at which iSVS system starts to reach the brain aspect of the subjects. (c) and (d) Estimating the two scattering decay slope rates a_1 and a_2, corresponding to the two different components of the head of the subjects, such has the scalp + skull layer and the dura mater + brain layer.

Figures 6(c) and 6(d) show the first a_1 and the second a_2 decay coefficients for each subject. As evident, human and rabbit subjects exhibit similar decay coefficients. The absolute value of the first decay coefficient is larger than that of the second, indicating that iSVS system suffers from more loss from the scalp + skull layer than from the dura mater + brain layer. This can be explained by the fact that increasing the S-D separation distance increase the depth of penetration until the brain component is attained. Then, further increase will not increase the depth of penetration by much but will rather increase the ratio of light attaining the brain component, as predicted by the numerical simulations [41–43].

Discussion

The relationship between the threshold distance S-D$_{th}$ and skin-to-brain depth appears to be nonlinear. At short skin-to-brain depths ($z < 1$ cm), as for rabbits, the ratio S-D$_{th}/z$ is around 2, indicating that a S-D$_{th}$ distance of twice the skin-to-brain depth is required to reach the brain component. At longer skin-to-brain depths ($z > 1$ cm), as for humans, the ratio S-D$_{th}/z$ approaches 1.

Those results are in line with prior research on depth sensitivity and source-to-detector separation in near-infrared spectroscopy (NIRS) for humans [39–43], where a "banana" spatial sensitivity profile is usually observed. As the S-D distance increases, the "banana" extends deeper into the brain, with deeper brain regions being more challenging to access [42]. The sensitivity was observed to decrease exponentially with the depth of penetration, and there exists a trade-off between greater sensitivity to deeper layers of the brain and signal-to-noise ratio (SNR).

Typically, a substantial gain in brain signal sensitivity can be observed while increasing short source-to-detector distances (S-D < 2.5 cm). However, as the S-D distance extends beyond 2.5 cm, the gains in sensitivity become progressively smaller, ultimately peaking at S-D > 3.5 cm. Beyond this point, further increasing the S-D distance yields diminishing returns in sensitivity to brain function. These findings underscore the importance of carefully selecting the source-to-detector distance.

As an example, CBF can be modulated through specific brain activation tasks like finger tapping, which induces changes in CBF that can be detected from the motor cortex. Investigating CBF changes during finger tapping using iSVS to measure brain activation tasks holds significant potential, offering new parameters and metrics for functional brain research [47,48]. It can complement functional MRI, which is often costly and time-consuming and may help traumatic brain injury detection, diagnosis, and recovery.

However, it is crucial to select the appropriate source-to-detector distance to ensure precise CBF detection. The results presented here offer valuable insights, allowing researchers to make informed decisions regarding the appropriate source-to-detector and to enhance the precision of CBF measurements during brain activation tasks.

Conclusion

We reported our investigations on the depth-sensitivity of laser interferometry speckle visibility spectroscopy (iSVS), where we varied the depth of penetration of the laser light into the head by tuning the source-to-detector distance, and identified the transition point at which CBF in humans and rabbits starts to be detected. A phantom experiment confirmed the results. Finally, we compared the skin-to-brain depth results measured from iSVS system with those measured from MRI and X-rays scans, both for humans and rabbits, and found that the skin-to-brain depths estimated from the MRI and X-rays scans agree with the measured iSVS S-D$_{th}$ distances. The relationship between S-D$_{th}$ and skin-to-brain depth appeared to be nonlinear, between short skin-to-brain depths ($z < 1$ cm) and long skin-to-brain depths (z > 1 cm).

By using the depth-sensitivity of iSVS, one can pinpoint the transition point at which CBF becomes detectable in humans. This method can serve as an assistive tool for craniotomy

surgeries, enhancing the precision and safety of the surgery by providing continuous, non-invasive monitoring of CBF dynamics [49,50]. A craniotomy is a surgical procedure, useful for treating the brain, in which a part of the skull is temporarily removed to gain direct access to the brain and its surrounding structures. For patients undergoing reconstructive skull surgery, the removed skull bone flap is replaced by a polymeric skull material acoustic window [51].

Post-craniotomy, the iSVS method can potentially be employed to scan and compare CBF on the operated side with the intact side, providing the medical team with essential follow-up information to optimize patient outcomes.

Appendix

A. Phantom experiment

In this section, we describe in detail the phantom experiment (corresponding to the results shown in Fig. 5(c)). Our phantom is composed of a liquid mixture. The liquid mixture was in a plastic cup, placed on an orbital shaker rotating at a speed of 60 rotations per minute, see picture in Fig. 5(c) and see Figs. 7(a) to 7(d). The source and detector fibers were mounted on a separate support, which was not moving and was placed above the cup, Fig. 7. Due to the rotating shaker, the liquid mixture in the cup was moving. During a single rotation, the iSVS system is measuring the change of decorrelation time in the liquid mixture from the rotation axis (center of the cup) to the outside layer (near the edge of the cup). The angular velocity of the rotating liquid mixture in the cup is changing along the horizontal line from the rotation axis, i.e., from the center to the edge of the cup [52].

By setting the orbital shaker at a speed of 60 rotations per minute, each second, the iSVS system is measuring the difference of angular velocities along the horizontal line, producing a liquid flow dynamic similar to the blood flow dynamic for humans, see Fig. 7 (e). For the
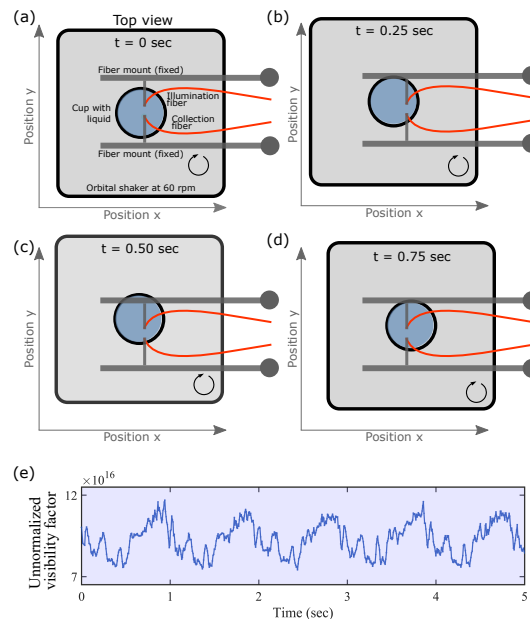

Fig. A1. I Experimental arrangement of the phantom experiment to mimic blood flow. A cup with a liquid was placed on a rotating orbital shaker at 60 rpm. (a)-(d) Top view of the experimental arrangement at different time (a) t = 0 sec (or also t = 1 sec), (b) t = 0.25 sec, (c) t = 0.50 sec and (d) t = 0.75 sec. (e) iSVS measurement of the liquid flow.

phantom experiment, the frequency freqHR was 1 Hz. The phantom in Fig. 6(c)-(d) "Milk" was made of 3% fat-milk and the one in Fig. 5(c) and Fig. 6(c)-(d) "Resin" was made with a mixture of 10% 3D printing resin and 90% water.

Disclosures. The authors declare no conflicts of interest.

Data availability. Data underlying the results presented in this paper are not publicly available at this time but may be obtained from the authors upon reasonable request.

References

1. L. Rangel-Castilla, J. Gasco, H. J. W. Nauta, D. O. Okonkwo, and C. S. Robertson, "Cerebral pressure autoregulation in traumatic brain injury," Neurosurgical Focus **25**(4), E7 (2008).
2. P. Liu, C. Xu, Z. Lin, S. Sur, Y. Li, S. Yasar, P. Rosenberg, M. Albert, and H. Lu, "Cerebrovascular reactivity mapping using intermittent breath modulation," NeuroImage **215**, 116787 (2020).
3. M. J. Ellis, L. N. Ryner, O. Sobczyk, J. Fierstra, D. J. Mikulis, J. A. Fisher, J. Duffin, W. Alan, and C. Mutch, "Neuroimaging assessment of cerebrovascular reactivity in concussion: current concepts, methodological considerations, and review of the literature," Front. Neurol. **7**, 61 (2016).
4. F. Calamante, D. L. Thomas, G. S. Pell, J. Wiersma, and R. Turner, "Measuring Cerebral Blood Flow Using Magnetic Resonance Imaging Techniques," J. Cereb. Blood Flow Metab. **19**(7), 701–735 (1999).
5. S. Sourbron, M. Ingrisch, A. Siefert, M. Reiser, and K. Herrmann, "Quantification of cerebral blood flow, cerebral blood volume, and blood–brain-barrier leakage with DCE-MRI," Magn. Reson. Med. **62**(1), 205–217 (2009).
6. J. A. Detre, D. C. Alsop, L. R. Vives, L. Maccotta, J. W. Teener, and E. C. Raps, "Noninvasive MRI evaluation of cerebral blood flow in cerebrovascular disease," Neurology **50**(3), 633–641 (1998).
7. M. E. Haveman, M. J. A. M. Van Putten, H. W. Hom, C. J. Eertman-Meyer, A. Beishuizen, and M. C. Tjepkema-Cloostermans, "Predicting outcome in patients with moderate to severe traumatic brain injury using electroencephalography," Crit Care **23**(1), 401 (2019).
8. F.J. Kirkham, T.S. Padayachee, S. Parsons, L.S. Seargeant, F.R. House, and R.G. Gosling, "Transcranial measurement of blood velocities in the basal cerebral arteries using pulsed Doppler ultrasound: Velocity as an index of flow," Ultrasound in Medicine & Biology **12**(1), 15–21 (1986).
9. M. Kehrer, R. Goelz, I. Krägeloh-Mann, and M. Schöning, "Measurement of volume of cerebral blood flow in healthy preterm and term neonates with ultrasound," Lancet **360**(9347), 1749–1750 (2002).
10. C. C. Bishop, S. Powell, D. Rutt, and N. L. Browse, "Transcranial Doppler measurement of middle cerebral artery blood flow velocity: a validation study," Stroke **17**(5), 913–915 (1986).
11. A. D. Edwards, J. S. Wyatt, C. Richardson, D. T. Delpy, M. Cope, and E. O. Reynolds, "Cotside measurement of cerebral blood flow in ill newborn infants by near infrared spectroscopy," Lancet **332**(8614), 770–771 (1988).
12. M. Diop, K. Verdecchia, T. Y. Lee, and K. St. Lawrence, "Calibration of diffuse correlation spectroscopy with a time-resolved near-infrared technique to yield absolute cerebral blood flow measurements," Biomed. Opt. Express **2**(7), 2068–2081 (2011).
13. E. M. Buckley, A. B. Parthasarathy, P. Ellen Grant, A. G. Yodh, and M. A. Franceschini, "Diffuse correlation spectroscopy for measurement of cerebral blood flow: future prospects," Neurophotonics **1**(1), 011009 (2014).
14. J. Li, G. Dietsche, D. Iftime, S. E. Skipetrov, G. Maret, T. Elbert, B. Rockstroh, and T. Gisler, "Noninvasive detection of functional brain activity with near-infrared diffusing-wave spectroscopy," J. Biomed. Opt. **10**(4), 044002 (2005).
15. M. N. Kim, T. Durduran, S. Frangos, B. L. Edlow, E. M. Buckley, H. E. Moss, C. Zhou, G. Yu, R. Choe, E. Maloney-Wilensky, R. L. Wolf, M. S. Grady, J. H. Greenberg, J. M. Levine, A. G. Yodh, J. A. Detre, and W. A. Kofke, "Noninvasive Measurement of Cerebral Blood Flow and Blood Oxygenation Using Near-Infrared and Diffuse Correlation Spectroscopies in Critically Brain-Injured Adults," Neurocrit. Care **12**(2), 173–180 (2010).
16. T. Durduran and A. G. Yodh, "Diffuse correlation spectroscopy for non-invasive, micro-vascular cerebral blood flow measurement," NeuroImage **85**, 51–63 (2014).
17. T. Durduran, G. Yu, M. G. Burnett, J. A. Detre, J. H. Greenberg, J. Wang, C. Zhou, and A. G. Yodh, "Diffuse optical measurement of blood flow, blood oxygenation, and metabolism in a human brain during sensorimotor cortex activation," Opt. Lett. **29**(15), 1766–1768 (2004).
18. S. Carp, D. Tamborini, D. Mazumder, K. C. Wu, M. Robinson, K. Stephens, O. Shatrovoy, N. Lue, N. Ozana, M. Blackwell, and M. A. Franceschini, "Diffuse correlation spectroscopy measurements of blood flow using 1064 nm light," J. Biomed. Opt. **25**(09), 097003 (2020).
19. J. Brake, M. Jang, and C. Yang, "Analyzing the relationship between decorrelation time and tissue thickness in acute rat brain slices using multispeckle diffusing wave spectroscopy," J. Opt. Soc. Am. A **33**(2), 270–275 (2016).
20. R. Bandyopadhyay, A. S. Gittings, S. S. Suh, P. K. Dixon, and D. J. Durian, "Speckle-visibility spectroscopy: A tool to study time-varying dynamics," Rev. Sci. Instrum. **76**(9), 093110 (2005).

21. C. P. Valdes, H. M. Varma, A. K. Kristoffersen, T. Dragojevic, J. P. Culver, and T. Durduran, "Speckle contrast optical spectroscopy, a non-invasive, diffuse optical method for measuring microvascular blood flow in tissue," Biomed. Opt. Express **5**(8), 2769–2784 (2014).

22. D. A. Boas and A. K. Dunn, "Laser speckle contrast imaging in biomedical optics," J. Biomed. Opt. **15**(1), 011109 (2010).

23. J. D. Briers, "Laser speckle contrast imaging for measuring blood flow," Optica Applicata **XXXVII**, 139–152 (2007).

24. A. Mazhar, D. J. Cuccia, T. B. Rice, S. A. Carp, A. J. Durkin, D. A. Boas, B. Choi, and B. J. Tromberg, "Laser speckle imaging in the spatial frequency domain," Biomed. Opt. Express **2**(6), 1553–1563 (2011).

25. A. K. Dunn, "Laser Speckle Contrast Imaging of Cerebral Blood Flow," Ann. Biomed. Eng. **40**(2), 367–377 (2012).

26. A. K. Dunn, H. Bolay, M. A. Moskowitz, and D. A. Boas, "Dynamic Imaging of Cerebral Blood Flow Using Laser Speckle," J. Cereb. Blood Flow Metab. **21**(3), 195–201 (2001).

27. Laser Institute of America, "American National Standards for safe use of lasers," ANSI Z136.1-2014 (2014). https://webstore.ansi.org/standards/lia/ansiz1362014.

28. J. Xu, A. K. Jahromi, and C. Yang, "Diffusing wave spectroscopy: A unified treatment on temporal sampling and speckle ensemble methods," APL Photonics **6**(1), 016105 (2021).

29. J. Xu, A. K. Jahromi, J. Brake, J. E. Robinson, and C. Yang, "Interferometric speckle visibility spectroscopy (iSVS) for human cerebral blood flow monitoring," APL Photonics **5**(12), 126102 (2020).

30. M. A. Wayne, E. J. Sie, A. C. Ulku, P. Mos, A. Ardelean, F. Marsili, C. Bruschini, and E. Charbon, "Massively parallel, real-time multispeckle diffuse correlation spectroscopy using a 500×500 SPAD camera," Biomed. Opt. Express **14**(2), 703–713 (2023).

31. W. Zhou, O. Kholiqov, S. P. Chong, and V. J. Srinivasan, "Highly parallel, interferometric diffusing wave spectroscopy for monitoring cerebral blood flow dynamics," Optica **5**(5), 518–527 (2018).

32. W. Zhou, O. Kholiqov, J. Zhu, M. Zhao, L. L. Zimmermann, R. M. Martin, B. G. Lyeth, and V. J. Srinivasan, "Functional interferometric diffusing wave spectroscopy of the human brain," Sci. Adv. **7**(20), eabe0150 (2021).

33. K. Murali and H. M. Varma, "Multi-speckle diffuse correlation spectroscopy to measure cerebral blood flow," Biomed. Opt. Express **11**(11), 6699–6709 (2020).

34. D. Mazumder, M. M. Wu, N. Ozana, D. Tamborini, M. A. Franceschini, and S. A. Carp, "Optimization of time domain diffuse correlation spectroscopy parameters for measuring brain blood flow," Neurophotonics **8**(3), 035005 (2021).

35. Y. X. Huang, S. Mahler, J. Mertz, and C. Yang, "Interferometric speckle visibility spectroscopy (iSVS) for measuring decorrelation time and dynamics of moving samples with enhanced signal-to-noise ratio and relaxed reference requirements," arXiv, arXiv:2306.17419 (2023).

36. O. Kholiqov, D. Borycki, and V. J. Srinivasan, "Interferometric near-infrared spectroscopy (iNIRS): performance tradeoffs and optimization," Opt. Express **25**(23), 28567–28589 (2017).

37. M. Robinson, D. Boas, S. Sakadžic, M. A. Franceschini, and S. Carp, "Interferometric diffuse correlation spectroscopy improves measurements at long source-detector separation and low photon count rate," J. Biomed. Opt. **25**(09), 097004 (2020).

38. S. Samaei, K. Nowacka, A. Gerega, Ż Pastuszak, and D. Borycki, "Continuous-wave parallel interferometric near-infrared spectroscopy (CW πNIRS) with a fast two-dimensional camera," Biomed. Opt. Express **13**(11), 5753–5774 (2022).

39. T. Myllylä, M. Harju, V. Korhonen, A. Bykov, V. Kiviniemi, and I. Meglinski, "Assessment of the dynamics of human glymphatic system by near-infrared spectroscopy," J. Biophotonics **11**(8), e201700123 (2018).

40. T. Myllylä, A. Popov, V. Korhonen, A. Bykov, and M. Kinnunen, "Optical sensing of a pulsating liquid in a brain-mimicking phantom," SPIE Proceedings, Diffuse Optical Imaging IV 8799, 87990X (2013).

41. F. B. Haeussinger, S. Heinzel, T. Hahn, M. Schecklmann, A. C. Ehlis, and A. J. Fallgatter, "Simulation of Near-Infrared Light Absorption Considering Individual Head and Prefrontal Cortex Anatomy: Implications for Optical Neuroimaging," PLoS One **6**(10), e26377 (2011).

42. G. E. Strangman, Z. Li, and Q. Zhang, "Depth Sensitivity and Source-Detector Separations for Near Infrared Spectroscopy Based on the Colin27 Brain Template," PLoS One **8**(8), e66319 (2013).

43. C. Mansouri, J. P. L'Huillier, and N. H. Kashou, "Depth sensitivity analysis of functional near-infrared spectroscopy measurement using three-dimensional Monte Carlo modelling-based magnetic resonance imaging," Lasers. Med. Sci. **25**(3), 431–438 (2010).

44. E. P. Goodwin and J. C. Wyant, "*Field Guide to Interferometric Optical Testing*," SPIE Press, (2006).

45. A. Doronin, C. Macdonald, and I. V. Meglinski, "Propagation of coherent polarized light in turbid highly scattering medium," J. Biomed. Opt. **19**(2), 025005 (2014).

46. A. Doronin, L. Tchvialeva, I. Markhvida, T. K. Lee, and I. Meglinski, "Backscattering of linearly polarized light from turbid tissue-like scattering medium with rough surface," J. Biomed. Opt. **21**(7), 071117 (2016).

47. S. M. Shams Kazmi, L. M. Richards, C. J. Schrandt, M. A. Davis, and A. K. Dunn, "Expanding applications, accuracy, and interpretation of laser speckle contrast imaging of cerebral blood flow," J. Cereb. Blood Flow Metab. **35**(7), 1076–1084 (2015).

48. L.-D. Liao, V. Tsytsarev, I. Delgado-Martínez, M.-L. Li, R. Erzurumlu, A. Vipin, J. Orellana, Y.-R. Lin, H.-Y. Lai, Y.-Y. Chen, and N. V. Thakor, "Neurovascular coupling: in vivo optical techniques for functional brain imaging," BioMed. Eng. OnLine **12**(1), 38 (2013).

49. A. Konovalov, V. Gadzhiagaev, F. Grebenev, D. Stavtsev, G. Piavchenko, A. Gerasimenko, D. Telyshev, I. Meglinski, and S. Eliava, "Laser Speckle Contrast Imaging in Neurosurgery: A Systematic Review," World Neurosurgery **171**, 35–40 (2023).

50. V. Kalchenko, I. Meglinski, A. Sdobnov, Y. Kuznetsov, and A. Harmelin, "Combined laser speckle imaging and fluorescent intravital microscopy for monitoring acute vascular permeability reaction," J. Biomed. Opt. **24**(06), 1 (2019).

51. C. Rabut, S. L. Norman, W. S. Griggs, J. J. Russin, K. Jann, V. Christopoulos, C. Liu, R. A. Andersen, and M. G. Shapiro, "A window to the brain: ultrasound imaging of human neural activity through a permanent acoustic window," bioRxiv, bioRxiv 2023.06.14.544094 (2023).

52. Z. Yan, L. Sun, J. Xiao, and Y. Lan, "The profile of an oil-water interface in a spin-up rotating cylindrical vessel," Am. J. Phys. **85**(4), 271–276 (2017).